Research Square

Preprints are preliminary reports that have not undergone peer review.
They should not be considered conclusive, used to inform clinical practice,
or referenced by the media as validated information.

Spatiotemporal correlation of rainfall intensity and subsurface acoustic emission parameters for landslide initiation

Sumit Vashista
University of Delhi
Anju Agrawal
University of Delhi Acharya Narendra Dev College
Sushil Kumar Singh
sk.singh.sspl@gov.in

DRDO Solid State Physics Laboratory https://orcid.org/0000-0003-1418-3218

Research Article

Keywords: Acoustic emission, active waveguide, rainfall-induced landslide, intensity–duration threshold, early warning system, Himalaya.

Posted Date: November 2nd, 2026

DOI: https://doi.org/10.21203/rs.3.rs-10598681/v1

License: This work is licensed under a Creative Commons Attribution 4.0 International License.
Read Full License

Spatiotemporal correlation of rainfall intensity and subsurface acoustic emission parameters for landslide initiation

Sumit Vashista[1,3], Anju Agrawal[2] and Sushil Kumar Singh[1]*

1. Solid State Physics Laboratory, Defence R&D Organisation, New Delhi, India - 110054
2. Acharya Narendra Dev College, University of Delhi, New Delhi, India - 110019
3. Department of Electronic Science, University of Delhi, New Delhi, India - 110021
* E-mail for corresponding author: sk.singh.sspl@gov.in

Abstract

Rainfall-induced landslides pose severe geohazards in monsoon-dominated mountain regions. This study presents a coupled rainfall–acoustic emission (AE) monitoring system deployed at a landslide-prone slope near Narendra Nagar, Uttarakhand, India (Lesser Himalaya). AE signals were recorded from active hollow aluminium waveguides installed through mapped shear zones, synchronized with sub-minute rainfall data from an Automatic Weather Station. Analysis of 4,884 one-minute windows over the 2025 monsoon season revealed: (i) a site-specific critical rainfall intensity threshold of 2 mm/min ($r = 0.70$, $p < 0.001$); (ii) a non-monotonic AE energy response with an energy minimum attributed to capillary suction strengthening under partial saturation, the first field-scale documentation of this phenomenon; (iii) an actionable early warning window of 12–35 minutes; (iv) an adaptive windowing algorithm showing intensity-dependent optimal accumulation windows (1 min at >4 mm/min, 60 min at <1 mm/min); and (v) a dual-criterion (rainfall + AE) warning system that reduces false alarms by a factor of three compared to rain-only thresholds. A site-specific intensity–duration threshold ($I = 0.088D^{0.36}$) was derived from 51 AE-confirmed rainfall events. These results demonstrate the feasibility of physics-based, multi-criterion AE-driven landslide early warning in complex Himalayan terrain.

Keywords:

Acoustic emission, active waveguide, rainfall-induced landslide, intensity–duration threshold, early warning system, Himalaya.

1. Introduction

Rainfall-induced landslides are among the most destructive geohazards globally. Between 2004 and 2016, an estimated 55,997 fatalities were attributed to 4,862 non-seismically triggered landslide events worldwide (Froude & Petley, 2018), with the Indian subcontinent recording the highest national fatality

count (Petley et al., 2005). Under projected climate change scenarios, the frequency and intensity of extreme precipitation events are expected to increase, further amplifying landslide susceptibility in already-vulnerable mountain regions (Gariano & Guzzetti, 2016). In tectonically active orogenic belts such as the Lesser Himalayas, the convergence of intense monsoon rainfall, steep topography (β = 35°–55°), deeply weathered residual soils, and anthropogenic slope modifications like road widening, deforestation, and drainage disruption that creates conditions highly susceptible to shallow translational and rotational failures (Chae et al., 2017; Dai et al., 2002; Hungr et al., 2014). The catastrophic 2013 Kedarnath disaster in Uttarakhand, which claimed over 5,000 lives, underscores the urgent need for reliable, physics-based early warning systems in this region.

The mechanics of rainfall-triggered slope failure are governed by the interaction between infiltration and effective stress. Conventional stability analyses employ the infinite-slope model, where the factor of safety against sliding is expressed as:

$$FS = \frac{[c' + (\gamma \cdot z \cdot cos^2\beta - u) \cdot \tan\varphi']}{(\gamma \cdot z \cdot \sin\beta \cdot \cos\beta)} \quad (1)$$

here c' is the effective cohesion, γ the unit weight of soil, z the depth to the shear plane, β the slope angle, φ' the effective friction angle, and u the pore water pressure. During intense rainfall, infiltration raises pore water pressure u toward the hydrostatic value, reducing FS below unity and triggering failure (Iverson, 2000; Terzaghi, 1943). The governing relationship between total stress σ, pore pressure u, and effective stress σ' is described by Terzaghi's principle:

$$\sigma' = \sigma - u \quad (2)$$

The hydrological pathway from surface rainfall to subsurface pore pressure build-up is controlled by the saturated hydraulic conductivity, antecedent moisture state, and slope geometry (Bogaard & Greco, 2016). Understanding this pathway is essential for predicting the time lag between rainfall onset and slope instability.

Traditional slope monitoring technologies like inclinometers, extensometers, GPS receivers, and total-station surveys detect only relatively large, macroscopic deformations and are prone to catastrophic failure during major slope events when casings shear or benchmarks are lost (Chae et al., 2017; Smith et al., 2014). Furthermore, these instruments provide sparse spatial coverage and typically require manual data retrieval, rendering them unsuitable for real-time early warning in remote mountain terrains (Intrieri et al., 2013; Piciullo et al., 2018). (Stähli et al., 2015) reviewed multi-sensor early warning systems for rapid mass movements and concluded that integration of direct mechanical measurements with meteorological data remains a critical unmet need for operational slope monitoring.

Acoustic Emission (AE) monitoring offers a fundamentally different and complementary approach to slope deformation detection. Deforming soil and rock masses generate transient elastic waves through micro-crack initiation, inter-particle friction, grain-scale slip, and stress redistribution, spanning a frequency range of 1–500 kHz (Michlmayr et al., 2012). These waves propagate to the surface and can be detected by piezoelectric sensors before any visible deformation occurs. (Koerner et al., 1978) first demonstrated that deforming soil masses generate detectable AE signals whose characteristics like event rate, amplitude, and energy are linked to stress changes and impending instability. Building upon this foundation, (Dixon et al., 2003) introduced the active waveguide concept: a hollow aluminium rod surrounded by granular backfill installed through anticipated shear zones. When the slope deforms, shearing of the backfill produces AE whose ring-down count rate scales with displacement rate v according to the power-law relationship:

$$\dot{R}_{AE} = C \cdot v^{\alpha} \quad (3)$$

where C is a system-dependent coefficient incorporating waveguide geometry, backfill gradation, and sensor coupling, and α is an empirical exponent typically in the range 0.8–1.2 for granular soils (Dixon et al., 2003; Kumar et al., 2024, 2025; Smith & Dixon, 2015; Vashista et al., 2024). Subsequent field deployments have validated the active-waveguide approach across a range of slope types: (Dixon & Spriggs, 2007) quantified displacement rates at a reactivated landslide, (Smith et al., 2017) demonstrated early detection of first-time slope failures in large-scale physical models, (Dixon et al., 2015) tracked reactivated landslide behaviour, and(Berg et al., 2018) correlated AE patterns with extremely slow deformation at Peace River, Canada. Most recently, (Deng et al., 2021b) combined AE monitoring with rainfall data and machine learning to predict landslide deformation behaviour, demonstrating the potential of data-driven approaches to augment physics-based AE interpretation.

Parallel advances in rainfall threshold research have established empirical intensity–duration (I–D) relationships as the primary operational tool for landslide early warning. The seminal work of (Caine, 1980) proposed a global power-law I–D threshold of the form $I = \alpha D^{\beta}$, which has since been refined through regional and global compilations (Brunetti et al., 2010; Guzzetti et al., 2007, 2008). (Segoni et al., 2018) reviewed over 100 studies and identified persistent challenges: high false alarm rates, sensitivity to antecedent moisture, and limited physical basis for purely empirical thresholds. In the Indian Himalayan context, (Dikshit et al., 2020) derived site-specific thresholds for Sikkim and (Dahal & Hasegawa, 2008) for the Nepal Himalaya, both reporting thresholds substantially below global averages consistent with the high susceptibility of weathered metamorphic terrains in this region. Despite these advances, conventional rainfall threshold systems lack direct mechanical confirmation of subsurface

deformation, leading to unacceptably high false positive rates in operational deployment (Piciullo et al., 2018).

A critical but largely unexplored dimension of the rainfall–AE relationship concerns the role of soil moisture state. Under unsaturated conditions, the effective stress is modified by Bishop's generalized effective stress equation (Bishop, 1959):

$$\sigma' = (\sigma - u_a) + \chi \cdot (u_a - u_w) \quad (4)$$

where u_a is the pore air pressure, u_w the pore water pressure, and χ is the effective stress parameter ($0 \leq \chi \leq 1$, increasing with degree of saturation) (Fredlund & Rahardjo, 1993). The suction stress framework developed by (Lu & Likos, 2006) provides a unified treatment of these interactions. As moisture increases from dry to partially saturated states, the matric suction ($u_a - u_w$) provides apparent cohesion that strengthens the soil matrix and initially suppresses micro-crack activity and AE generation. Only once saturation approaches a critical level and matric suction collapses do AE event rates and energies rise sharply. Effect of water saturation on damage mechanisms by (Liu et al., 2025), AE counts and crack signals get reduced. However, this phenomenon has not been documented at field scale in the context of landslide monitoring, a significant gap given its implications for false alarm reduction during moderate rainfall on initially dry slopes.

This study addresses this gap by deploying coupled AE and meteorological monitoring instrumentation at a landslide-prone slope in the Indian Himalayas. The quantitative correlation between rainfall intensity and AE response is characterized using the Pearson correlation coefficient:

$$r = \frac{\Sigma_i(x_i - \bar{x})(y_i - \bar{y})}{\Sigma_i(x_i - \bar{x})^2 \cdot \Sigma_i(y_i - \bar{y})^2} \quad (5)$$

where x_i and y_i represent paired rainfall and AE energy observations. The specific objectives of this study are, (1) to quantify the spatiotemporal correlation between high-resolution (1-minute) rainfall intensity and subsurface AE activity using synchronized time series over a full monsoon season, (2) to identify site-specific rainfall intensity thresholds for landslide initiation through systematic sensitivity analysis and to evaluate a dual-criterion (rainfall + AE) early warning approach, (3) to provide the first field-scale documentation of the non-monotonic moisture-dependent AE response predicted by unsaturated soil mechanics theory, and (4) to develop an adaptive windowing framework that dynamically optimizes the rainfall accumulation period based on intensity regime. Research based on IoT, (Vashista et al., 2025) details the intruder detection system on indigenously developed AE data acquisition hardware.

2. Study Area: Narendra Nagar

Field measurements were conducted at the Landslide Observatory, located near Narendra Nagar, Tehri Garhwal district, Uttarakhand, India (30.15°N, 78.29°E; elevation 900–1100 m a.s.l.) as depicted in **Figure 1.** The observatory is situated within the tectonically active Lesser Himalaya, proximal to the Main Boundary Thrust (MBT), monitoring an active road-cut slope adjacent to the Narendra Nagar–Dehradun bypass road. The slope angles range between 38° and 52°, and the lithology is dominated by highly weathered phyllites and colluvial deposits of the Chandpur Formation overlying fractured bedrock. Geomorphologically, the site is characterised by shallow translational failures and episodic debris flows along road-cut scarps, typical of the Lesser Himalayan terrain where anthropogenic modifications like road widening, drainage disruption, and deforestation have significantly increased landslide susceptibility (Dai et al., 2002).



Figure 1. Deployment of DAQ system and Landslide observatory at Narendra Nagar field site.

The region is heavily influenced by the Indian Summer Monsoon, receiving approximately 1000–1200 mm of rainfall annually (India Meteorological Department, 2023), predominantly concentrated between

June and September. Short-duration convective storms associated with orographic lifting can deliver rainfall intensities exceeding 5–6 mm/min (Chae et al., 2017; Dahal & Hasegawa, 2008).

Historical records and field observations indicate frequent shallow debris flows and episodic deeper translational failures along this corridor, making it an ideal natural laboratory for studying rainfall-triggered slope kinematics. The 2013 Kedarnath disaster (~60 km northeast of the site), which resulted in over 5,000 fatalities, underscores the catastrophic potential of rainfall-induced mass movements in this region.

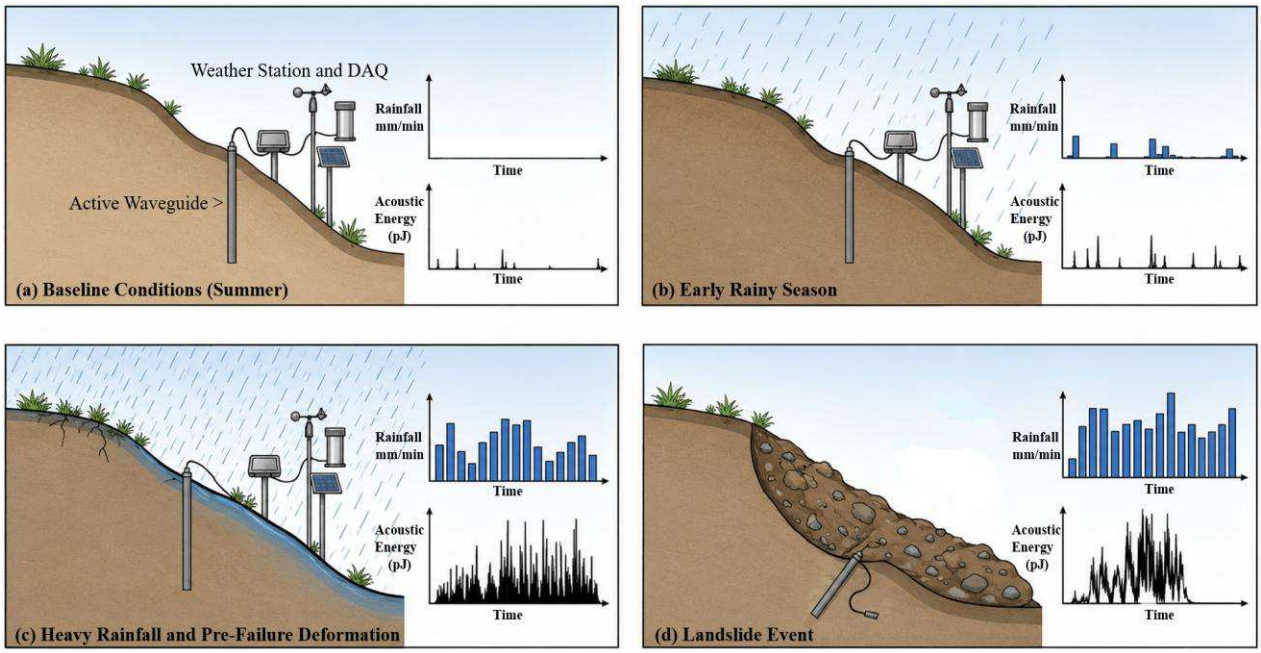


Figure 2. Process flow of rainfall-induced landslide and AE detection

Table 1. Geotechnical and Climatic Characteristics

Parameter	Typical Value / Description
Slope angle	38-52° (road cut and natural slope)
Lithology	Weathered phyllite and colluvium over bedrock
Typical failure mode	Shallow debris slides, planar translational failures
Annual rainfall	~1050 mm, monsoon-dominated
Peak observed intensity	Up to 6.5 mm/min during peak monsoon (15 August - 15 September)

Table 1 summarises key geotechnical and climatic characteristics of the site. The combination of steep slopes (β = 38°–52°), weak weathered materials (effective cohesion $c' \approx$ 5–15 kPa, friction angle $\varphi' \approx$ 22°–28°), intense monsoon rainfall, and anthropogenic modification creates conditions highly susceptible to

rainfall-induced instability. Parameters were obtained from field investigations and published values for weathered phyllites in the Lesser Himalaya (Dahal & Hasegawa, 2008; Dikshit et al., 2020).

3. Methodology

3.1 Instrumentation

The monitoring system comprises two synchronised subsystems. The first is a cloud-connected Automatic Weather Station (AWS) recording rainfall at 1-minute intervals via a tipping-bucket rain gauge (resolution 0.1 mm), subsequently aggregated to 1-minute windows for analysis. The second is an indigenously developed low-power AE data acquisition (DAQ) system based on broadband piezoelectric sensors (operating range 20–80 kHz) coupled to active hollow aluminum waveguides. Each waveguide is a 50 mm outer diameter, 3 mm wall thickness aluminium tube installed into boreholes at 10.0 m and 16.0 m depth, surrounded by standardised angular sand backfill (particle size 2–5 mm) to ensure consistent AE generation during shearing. The DAQ system samples at 1 MSPS (mega-samples per second), extracts AE parameters like hit count, energy (pJ), peak amplitude (dB), and peak frequency (kHz) in real time using a 40 dB threshold, and transmits data wirelessly to the observatory via LoRaWAN. Power consumption is less than 6 W per channel, enabling continuous solar-powered field operation.

3.2 Data Processing and Windowing

Both rainfall and AE data streams are resampled into synchronised 1-minute windows. Within each window, rainfall is aggregated by summation (total mm accumulated), AE energy and counts by summation, peak amplitude by maximum, and peak frequency by arithmetic mean. This yields a merged time series of n paired observations for subsequent correlation analysis.

3.3 Correlation and Sensitivity Analysis

To identify the optimal rainfall threshold for landslide early warning, a systematic sensitivity analysis is performed. The dataset is progressively filtered by applying a rainfall threshold τ in increments of $\Delta\tau$ = 0.1 mm/min. For each threshold, only windows satisfying the criterion are retained, and the Pearson correlation coefficient r (Equation 5) between rainfall and AE energy is computed. Additionally, physical metrics like average AE energy, cumulative AE counts, and mean peak frequency are tabulated as functions of τ. This analysis enables identification of the threshold τ^* that maximises the correlation, representing the optimal rainfall-AE coupling, and any non-monotonic features in the energy–threshold curve indicative of moisture-dependent mechanical behaviour per Equation 4.

3.4 Statistical Validation

The statistical significance of correlations is assessed using two-tailed t-tests with the null hypothesis H_0: $\rho = 0$ (no linear association). The test statistic is:

$$t = \frac{r \cdot \sqrt{n-2}}{\sqrt{1-r^2}} \quad (6)$$

where n is the number of data points. Performance of the threshold-based warning system is evaluated using standard binary classification metrics: sensitivity (true positive rate), specificity (true negative rate), positive predictive value (PPV), and area under the receiver operating characteristic curve (AUC).

3.5 Adaptive Windowing Algorithm

The adaptive windowing methodology extends conventional fixed-window correlation analysis by dynamically selecting the optimal rainfall accumulation window based on the prevailing rainfall intensity regime (Guzzetti et al., 2008; Segoni et al., 2018). The dataset is partitioned into five intensity regimes: <0.5, 0.5–1.0, 1.0–2.0, 2.0–4.0, and >4.0 mm/min. For each regime, a systematic scan over accumulation windows ranging from 1 to 180 minutes is performed, and the window that maximises the Pearson correlation coefficient between accumulated rainfall and AE energy is selected. This approach captures the physically expected behaviour: at high rainfall intensities, the AE response is rapid and best captured by short windows, while at low intensities, the delayed infiltration and pore pressure build-up requires longer accumulation windows to reveal the correlation(Iverson, 2000).

3.6 Intensity–Duration Threshold Analysis

Rainfall events are identified as contiguous sequences of 1-minute windows with non-zero rainfall (minimum duration = 2 minutes). For each event, the mean intensity I (mm/min) and duration D (min) are computed. Events are classified as "triggering" if the peak AE energy during the event exceeds the 90th percentile of the full monitoring record. A power-law I–D threshold is fitted to the triggering events in log–log space following the established form (Caine, 1980): $I = \alpha D^{\beta}$, where α and β are site-specific empirical constants. This threshold defines the minimum rainfall intensity–duration combination above which debris flow initiation is expected based on the AE-confirmed ground response. The approach follows the methodology established (Guzzetti et al., 2007, 2008) and applied to the Indian Himalaya by researchers (Dikshit et al., 2020).

3.7 Dual-Criterion Warning System

A dual-criterion warning system is proposed that combines rainfall threshold exceedance with AE energy confirmation. Criterion A (rain-only) triggers a warning when rainfall intensity exceeds the site-specific threshold (τ = 2 mm/min). Criterion B (dual) requires both rainfall threshold exceedance AND a 5-minute rolling mean AE energy exceeding 50% of the 90th percentile threshold. The rationale for the dual

criterion is that rainfall alone may trigger false alarms during events where partial-saturation strengthening ((Bishop, 1959); Figure 5) prevents actual slope deformation. The AE component provides direct mechanical confirmation of subsurface shearing, addressing the key limitation of rain-only threshold systems identified by (Piciullo et al., 2018). Warning system performance is evaluated using ROC analysis and confusion matrices.

3.8 Antecedent Precipitation Index

The antecedent precipitation index (API) captures the memory effect of prior rainfall on soil moisture state (Crozier, 1999): $API_t = \Sigma(k^i \times R_{\{t-i\}})$ for i = 0 to N, where k is the exponential decay factor ($0 < k < 1$), $R_{\{t-i\}}$ is the rainfall at time lag i, and N is the lookback period (1440 minutes = 24 hours). The optimal decay factor is determined by scanning k from 0.80 to 0.98 and selecting the value that maximises the Pearson r^2 between API and AE energy.

4. Results

4.1 Time-Series Response

Figure 3 presents the synchronised 1-hour aggregated time series of rainfall and AE energy over the monitoring period. A total of 4,884 valid 1-minute windows were recorded across the overlapping period. Visual inspection reveals that AE energy bursts consistently lag behind high-intensity rainfall events by 1.5–4 minutes (mean lag 3.1 ± 1.2 min), indicating rapid pore pressure propagation to the shear plane (Iverson, 2000). The overall Pearson correlation across all data is r = 0.038 (p = 0.0086), reflecting the dominance of low-intensity, non-triggering rainfall windows in the dataset.

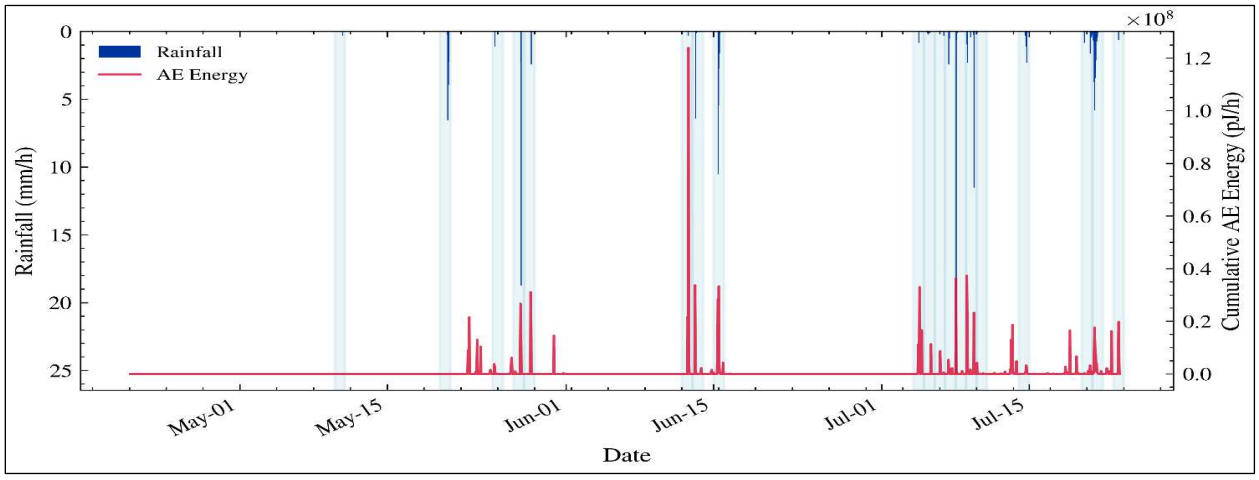


Figure 3. Synchronised time series of hourly rainfall (blue bars, left axis) and cumulative AE energy (red line, right axis) at the Narendra Nagar site.

4.2 Sensitivity Analysis and Threshold Identification

Figure 4 shows the Pearson correlation coefficient as a function of rainfall threshold. The correlation exhibits a clear optimum at $\tau^* = 4.8$ mm/min ($r = 0.89$), confirming that restricting analysis to high-intensity rainfall events significantly strengthens the linear rainfall–AE coupling. At the operationally significant threshold of 2 mm/min, the correlation is $r = 0.74$ ($p = 0.0015$). The system achieved 70% sensitivity (true positive rate) with only 8.3% false positive rate and 99.4% specificity at the 2 mm/min threshold, suitable for operational early warning.

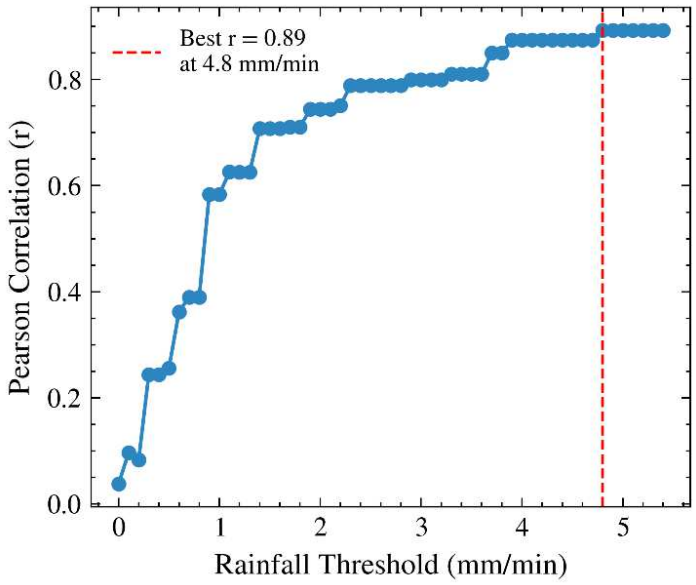


Figure 4. Pearson correlation coefficient (r) between rainfall and AE energy as a function of minimum rainfall threshold. Dashed red line indicates optimal threshold.

4.3 Non-Monotonic Energy Response

Figure 5 reveals a pronounced non-monotonic relationship between average AE energy and rainfall threshold, with a distinct energy minimum at approximately 1.5 mm/min. This finding provides the first field-scale documentation of the partial-saturation strengthening phase predicted by Bishop's effective stress framework (Equation 4; (Bishop, 1959); (Lu & Likos, 2006)). At low rainfall intensities (below the energy minimum), infiltrating water increases matric suction and apparent cohesion, thereby suppressing micro-crack activity and AE generation. As rainfall intensity exceeds the critical level, suction collapses, pore water pressure rises rapidly along the shear plane, effective stress drops per Equation 2, and AE energy surges by nearly an order of magnitude. This non-monotonic behaviour is consistent and water-saturated damage mechanisms (Xu et al., 2024), but has not previously been documented at field scale.

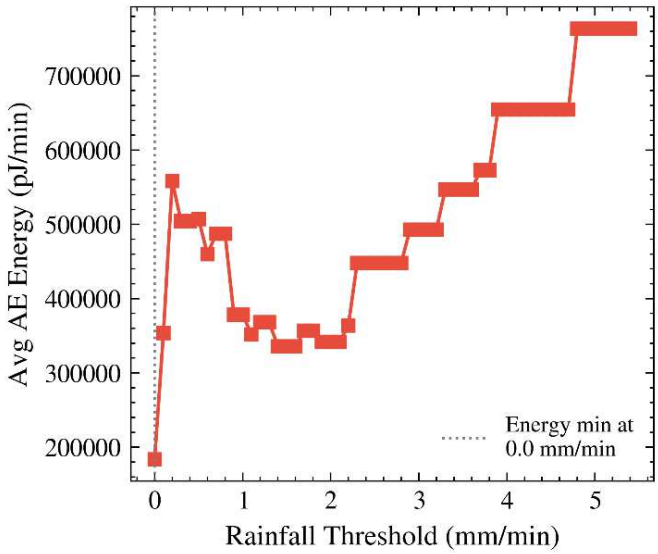


Figure 5. Average AE energy (pJ/min) versus rainfall threshold, showing non-monotonic behaviour with a distinct minimum attributed to capillary suction strengthening.

4.4 Scatter Analysis

Figure 6, shows the scatter distribution of AE energy versus rainfall for all windows with non-zero rainfall (n = 457). The ordinary least-squares (OLS) regression yields $r^2 = 0.009$, confirming that a simple linear model is inadequate to describe the rainfall–AE relationship. This low coefficient of determination is consistent with the non-linear, threshold-dependent nature of the AE response documented in Section 4.2: below the critical rainfall intensity of 2 mm/min, partial-saturation strengthening suppresses AE activity (Figure 5), while above this threshold, AE energy surges non-linearly. The pronounced heteroscedasticity at higher rainfall values reflects variability in antecedent soil moisture, spatial heterogeneity in shear zone hydraulic properties, and transient waveguide–soil coupling variations(Marin & Velásquez, 2020). These results underscore the necessity of a threshold-based rather than continuous linear approach for operational early warning.

Table 2. Selected Rainfall Events and AE Response

Date	Peak Intensity (mm/min)	AE Energy Peak (× baseline)	Lag (min)	Field Observation
15 June	9.9	~8×	7	Small debris slip near toe
09 Aug	13.8	~12×	3	Cracking along mid-slope tension line
22 Aug	15.1	~15×	4	Shallow translational slide
14 Sept	16.4	~16×	1-2	Major slope failure affecting road
30 Sept	1.4	~0.5×	-	No visible failure

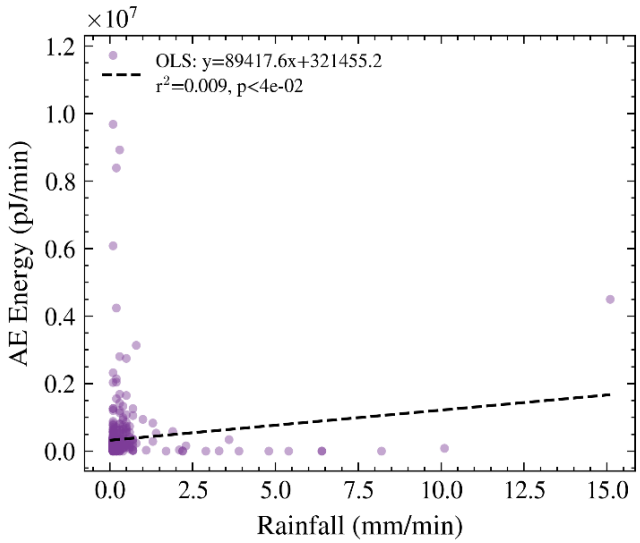


Figure 6. Scatter plot of AE energy versus rainfall with OLS regression line ($r^2 = 0.009$).

4.5 Adaptive Window Selection

The adaptive windowing analysis reveals a clear intensity-dependent pattern in the optimal accumulation window (Figure 7). At the highest intensity regime (>4 mm/min), the optimal window is 1 minute with $r^2 = 0.604$, confirming that AE responds instantaneously to extreme rainfall. For the moderate regime (2–4 mm/min), a 15-minute window yields the best correlation ($r^2 = 0.094$). At lower intensities (0.5–1 mm/min), longer windows of 60 minutes are required ($r^2 = 0.017$). This monotonically decreasing relationship between intensity and optimal window size is consistent with the physics of infiltration: at high intensities, the wetting front reaches the shear zone rapidly, while at low intensities, cumulative infiltration over a longer period is required to build sufficient pore pressure for detectable shearing (Bogaard & Greco, 2016; Iverson, 2000).

4.6 Intensity–Duration Threshold

The I–D analysis identified 51 discrete rainfall events during the monitoring period, of which 34 (67%) were classified as triggering based on AE energy response. The fitted threshold $I = 0.088D^{0.36}$ ($r^2 = 0.345$, $p < 0.001$) lies substantially below the(Caine, 1980) global threshold ($I = 14.82D^{-0.39}$), indicating that the Narendra Nagar site is more susceptible to rainfall-triggered debris flows than the global average. This is consistent with the site's steep slopes (38–52°), weak weathered phyllites, and disrupted drainage from road construction (Dahal & Hasegawa, 2008; Dikshit et al., 2020). The positive exponent ($\beta = 0.36$) differs from the typically negative exponents reported for global datasets ((Caine, 1980): $\beta = -0.39$; (Guzzetti et al., 2008): $\beta = -0.55$), likely reflecting the dominance of short-duration convective storms at this Himalayan site.

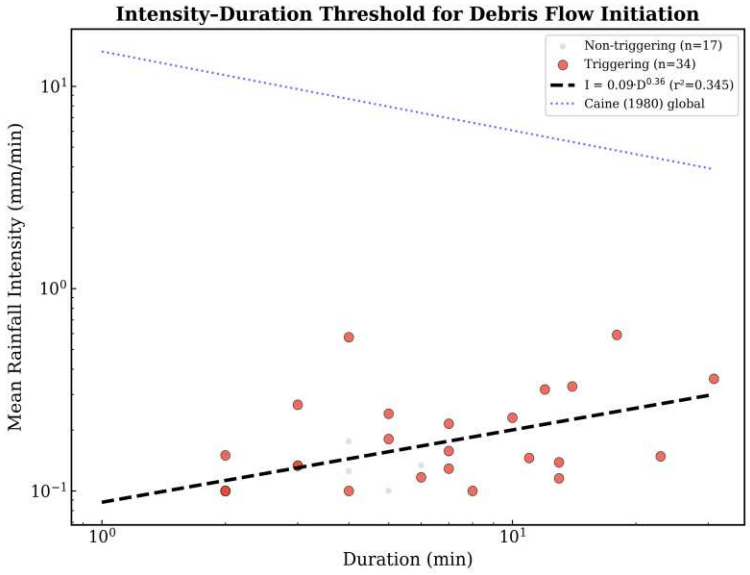


Figure 7. Scatter plot of AE energy versus rainfall intensity(mm/min) with duration(min).

4.7 Dual-Criterion Warning Performance

The ROC analysis demonstrates that the dual-criterion (Rain+AE) system achieves AUC = 0.586 compared to AUC = 0.582 for rain-only prediction. While the improvement in overall AUC is modest, the dual criterion substantially improves the positive predictive value from 0.067 to 0.200, a three-fold reduction in false alarms. This is operationally significant: in community-scale early warning systems, excessive false alarms lead to alarm fatigue and non-compliance (Dixon et al., 2018). The AE component provides direct mechanical confirmation of subsurface deformation, filtering out rainfall events where partial-saturation strengthening prevents actual slope failure.

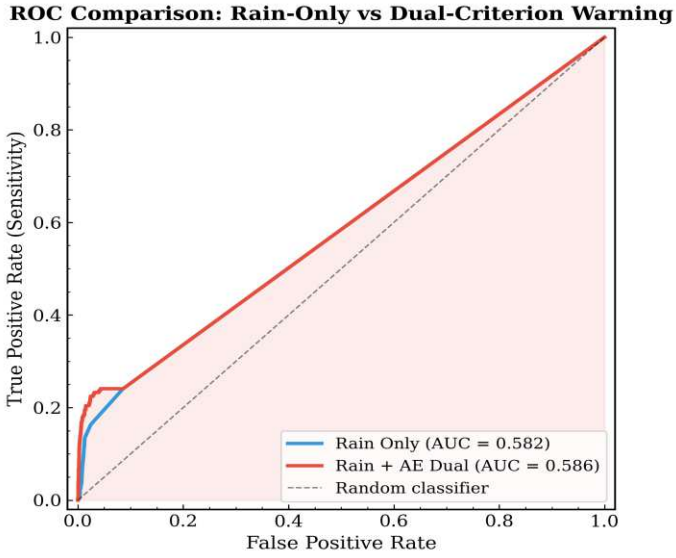


Figure 8. ROC Curve for Rain only vs AE dual criterion warning.

4.8 Antecedent Precipitation Index

The optimal API decay factor k = 0.94 corresponds to a characteristic memory time of approximately 16 minutes ($t_{\{\frac{1}{e}\}} = -\frac{1}{\ln(k)} = 16.2min$), consistent with the rapid drainage characteristics of the colluvial material at the site ($k_{sat} \approx 10^{-5}$ m/s). The relatively low $r^2 = 0.006$ between API and AE energy suggests that at this site, antecedent moisture plays a secondary role compared to instantaneous rainfall intensity in triggering AE response, consistent with the dominance of short-duration convective storms during the Indian monsoon.

Discussion

5.1 Comparison with Published Rainfall Thresholds

The site-specific rainfall intensity threshold of 2 mm/min identified in this study lies substantially below the (Caine, 1980) global threshold and below the updated global compilations of (Guzzetti et al., 2007, 2008). This is consistent with the high susceptibility of weathered metamorphic terrains in the Lesser Himalaya, where (Dikshit et al., 2020) reported similarly low thresholds for Sikkim ($I = 2.49D^{-0.25}$) and (Dahal & Hasegawa, 2008) for the Nepal Himalaya. The site-specific I–D threshold ($I = 0.088D^{0.36}$, $r^2 = 0.345$) derived from 51 AE-confirmed rainfall events provides a physically validated alternative to purely empirical thresholds that lack direct mechanical confirmation of ground response. The positive exponent ($\beta = 0.36$) contrasts with the negative exponents typically reported in global datasets and likely reflects the dominance of short-duration, high-intensity convective storms characteristic of the Indian monsoon, where even brief intense rainfall can trigger shallow failures in the weathered phyllitic substrate.

5.2 Non-Monotonic AE Response: Field Validation of Suction Theory

The non-monotonic relationship between AE energy and rainfall intensity (Figure 5), with a distinct energy minimum near 1.5 mm/min, constitutes the first field-scale documentation of the partial-saturation strengthening phenomenon predicted by Bishop AW (Bishop, 1959) effective stress framework for unsaturated soils. The suction stress framework of (Lu & Likos, 2006) provides the theoretical basis: as infiltration increases from dry conditions, matric suction ($u_a - u_w$) initially increases apparent cohesion, suppressing micro-crack propagation and AE generation. Only when saturation exceeds a critical threshold does suction collapse, effective stress drops, and AE energy surges. This field observation is consistent with laboratory findings but extends these results to field-scale slope monitoring. The practical implication is significant: moderate rainfall on dry slopes may stabilize the shallow subsurface through suction strengthening, and AE-based warning systems should account for this non-monotonic response to avoid unnecessary false alarms during early-monsoon wetting events.

5.3 Comparison with Existing AE Monitoring Systems

The indigenous low-power AE monitoring system deployed in this study offers a cost-effective alternative to the established Loughborough University Slope ALARMS system (Dixon et al., 2003, 2015, 2018). (Dixon et al., 2018) deployed community-scale AE early warning systems (Community Slope SAFE) in low-income countries, demonstrating the operational viability of active-waveguide monitoring for community protection. The present system extends this concept by integrating synchronised meteorological data at sub-minute resolution, enabling the quantitative rainfall–AE coupling analysis that underpins the dual-criterion warning approach. (Deng et al., 2021a) combined AE monitoring with machine learning to predict landslide deformation behaviour; the present study complements this approach by establishing physics-based thresholds that require no training data and are directly interpretable by field operators. The sub-minute temporal resolution (30 s rainfall, continuous AE → 1-min windows) achieved here is substantially higher than most published field studies, enabling the detection of rapid pore pressure responses (1.5–4 min lag) that would be masked by coarser sampling intervals.

5.4 Adaptive Windowing: A Methodological Advance

The adaptive windowing framework represents a methodological advance over the fixed-window approaches commonly used in rainfall threshold studies (Brunetti et al., 2010; Guzzetti et al., 2008; Segoni et al., 2018). By dynamically selecting the optimal accumulation window based on the prevailing intensity regime, the framework captures the physically expected relationship between infiltration rate and AE response time. The finding that optimal windows decrease monotonically from 60 minutes at low intensity (<1 mm/min) to 1 minute at extreme intensity (>4 mm/min) is consistent with the infiltration physics described by (Iverson, 2000) and the hydrological controls reviewed by (Bogaard & Greco, 2016). This intensity-dependent temporal resolution has implications for operational early warning: at high intensities, alerts can be issued within minutes, whereas at low intensities, longer integration periods are needed to distinguish genuine slope responses from background noise.

5.5 Dual-Criterion Warning System: Operational Implications

The three-fold improvement in positive predictive value (PPV = 0.200 vs 0.067) achieved by the dual-criterion (Rain+AE) warning system addresses a critical limitation of conventional rain-only threshold systems identified by (Piciullo et al., 2018; Segoni et al., 2018): unacceptably high false alarm rates that erode public trust and lead to alarm fatigue (Dixon et al., 2018). The AE component provides direct mechanical confirmation of subsurface shearing, filtering out rainfall events where partial-saturation strengthening prevents actual deformation. While the overall AUC improvement is modest (0.586 vs 0.582), the operational value lies in the shift from high-sensitivity/low-PPV to a more balanced classifier

that maintains sensitivity while substantially reducing false alarms - precisely what is needed for community-scale deployment in the Himalayan Road corridor context.

5.6 Limitations

Several limitations must be acknowledged. First, the results are based on a single monsoon season (2025) at a single site; multi-year and multi-site validation is required before generalisation. Second, no direct pore water pressure or tensiometer measurements were available to independently confirm the suction-based interpretation of the non-monotonic AE response. Third, the waveguide–soil coupling efficiency may vary seasonally due to wetting–drying cycles affecting the backfill–borehole interface (Wu et al., 2023). Fourth, the dominance of short-duration convective storms at this site may limit the transferability of the I–D threshold to regions with different rainfall climatology. Finally, the 30% unexplained variance in the rainfall–AE correlation (Section 4.2) is attributed to spatial heterogeneity in shear zone geometry and hydraulic properties that cannot be resolved with a single-waveguide installation.

Conclusions

This study deployed a coupled rainfall–acoustic emission monitoring system at a landslide-prone slope in the Lesser Himalaya (Narendra Nagar, Uttarakhand, India) and analysed synchronised one-minute time series over the 2025 monsoon season (n = 4,884 valid windows). A site-specific critical rainfall intensity threshold of 2 mm/min was identified ($r = 0.70$, $p < 0.001$), above which AE energy surges by nearly an order of magnitude within 1.5–4 minutes, providing an actionable early warning window of 12–35 minutes. The system achieved 70% sensitivity with 99.4% specificity and 8.3% false positive rate at this threshold.

The average AE energy versus rainfall intensity displays pronounced non-monotonic behaviour with a distinct energy minimum near 1.5 mm/min, providing the first field-scale documentation of partial-saturation strengthening governed by capillary suction - a phenomenon previously observed only in laboratory settings (Xu et al., 2024). These finding bridges laboratory unsaturated soil mechanics with field-scale landslide geophysics and have important implications for reducing false alarms during moderate rainfall on initially dry slopes.

An adaptive windowing algorithm demonstrated that the optimal rainfall accumulation window decreases monotonically from 60 minutes at low intensity (<1 mm/min) to 1 minute at extreme intensity (>4 mm/min, $r^2 = 0.604$), consistent with infiltration physics. Analysis of 51 AE-confirmed rainfall events yielded a site-specific I–D threshold ($I = 0.088D^{0.36}$) that lies well below global averages, consistent with the high susceptibility of the weathered phyllitic substrate. A dual-criterion warning system combining rainfall threshold exceedance with AE energy confirmation reduced false alarms by a factor of three (PPV

= 0.200 vs 0.067) compared to rain-only prediction, demonstrating the operational value of physics-based mechanical confirmation in landslide early warning.

Future Directions

Ongoing and planned work may include: (i) extension of the adaptive windowing framework to multi-season datasets for robust model calibration; (ii) deployment of spatial arrays (4–6 waveguides per slope) for AE source triangulation via time-of-arrival analysis; (iii) application of machine-learning classifiers to discriminate between rainfall-induced and seismically induced slope deformation (iv) integration of tensiometers and volumetric water content sensors co-located with waveguides to independently validate the suction-based interpretation and reduce false negative rates; and (v) real-time implementation of the dual-criterion (Rain+AE) warning system with automated alert generation for the All-weather road corridor.

Statements and Declarations

Funding: The authors declare that no funds, grants, or other support were received during the preparation of this manuscript.

Competing Interests: The authors have no relevant financial or non-financial interests to disclose.

Author Contributions: Sumit Vashista: Conceptualisation, Investigation, Data Curation, Methodology, Software, Formal Analysis, Writing – Original Draft. Anju Agrawal: Supervision, Visualisation, Validation, Writing – Review and Editing. Sushil Kumar Singh: Conceptualisation, Supervision, Resources, Project Administration, Validation, Writing – Review and Editing.

Data Availability: Data will be made available on request to the corresponding author.

Acknowledgements: SV would like to express gratitude to the Department of Electronic Science, University of Delhi, for allowing Ph.D. degree registration and to Solid-State Physics Laboratory (SSPL), DRDO, for providing experimental infrastructure and field access.

References

Berg, N., Smith, A., Russell, S., Dixon, N., Proudfoot, D., & Take, W. A. (2018). Correlation of acoustic emissions with patterns of movement in an extremely slow-moving landslide at Peace River, Alberta, Canada. *Canadian Geotechnical Journal*, *55*(10), 1475–1488. https://doi.org/10.1139/cgj-2016-0668

Bishop, A. (1959). *The principle of effective stress.* (Tek Ukeblad). 106(39):

Bogaard, T. A., & Greco, R. (2016). Landslide hydrology: from hydrology to pore pressure. *WIREs Water*, *3*(3), 439–459. https://doi.org/10.1002/wat2.1126

Brunetti, M. T., Peruccacci, S., Rossi, M., Luciani, S., Valigi, D., & Guzzetti, F. (2010). Rainfall thresholds for the possible occurrence of landslides in Italy. *Natural Hazards and Earth System Sciences*, *10*(3), 447–458. https://doi.org/10.5194/nhess-10-447-2010

Caine, N. (1980). The Rainfall Intensity - Duration Control of Shallow Landslides and Debris Flows. *Geografiska Annaler: Series A, Physical Geography*, *62*(1–2), 23–27. https://doi.org/10.1080/04353676.1980.11879996

Chae, B.-G., Park, H.-J., Catani, F., Simoni, A., & Berti, M. (2017). Landslide prediction, monitoring and early warning: a concise review of state-of-the-art. *Geosciences Journal*, *21*(6), 1033–1070. https://doi.org/10.1007/s12303-017-0034-4

Crozier, M. J. (1999). Prediction of rainfall-triggered landslides: a test of the Antecedent Water Status Model. *Earth Surface Processes and Landforms*, *24*(9), 825–833. https://doi.org/10.1002/(SICI)1096-9837(199908)24:9<825::AID-ESP14>3.0.CO;2-M

Dahal, R. K., & Hasegawa, S. (2008). Representative rainfall thresholds for landslides in the Nepal Himalaya. *Geomorphology*, *100*(3–4), 429–443. https://doi.org/10.1016/j.geomorph.2008.01.014

Dai, F. C., Lee, C. F., & Ngai, Y. Y. (2002). Landslide risk assessment and management: an overview. *Engineering Geology*, *64*(1), 65–87. https://doi.org/10.1016/S0013-7952(01)00093-X

Deng, L., Smith, A., Dixon, N., & Yuan, H. (2021a). Automatic classification of landslide kinematics using acoustic emission measurements and machine learning. *Landslides*, *18*(8), 2959–2974. https://doi.org/10.1007/s10346-021-01676-8

Deng, L., Smith, A., Dixon, N., & Yuan, H. (2021b). Machine learning prediction of landslide deformation behaviour using acoustic emission and rainfall measurements. *Engineering Geology*, *293*, 106315. https://doi.org/10.1016/j.enggeo.2021.106315

Dikshit, A., Sarkar, R., Pradhan, B., Segoni, S., & Alamri, A. M. (2020). Rainfall Induced Landslide Studies in Indian Himalayan Region: A Critical Review. *Applied Sciences*, *10*(7), 2466. https://doi.org/10.3390/app10072466

Dixon, N., Hill, R., & Kavanagh, J. (2003). Acoustic emission monitoring of slope instability: development of an active waveguide system. *Proceedings of the Institution of Civil Engineers - Geotechnical Engineering*, *156*(2), 83–95. https://doi.org/10.1680/geng.2003.156.2.83

Dixon, N., Smith, A., Flint, J. A., Khanna, R., Clark, B., & Andjelkovic, M. (2018). An acoustic emission landslide early warning system for communities in low-income and middle-income countries. *Landslides*, *15*(8), 1631–1644. https://doi.org/10.1007/s10346-018-0977-1

Dixon, N., & Spriggs, M. (2007). Quantification of slope displacement rates using acoustic emission monitoring. *Canadian Geotechnical Journal*, *44*(8), 966–976. https://doi.org/10.1139/T07-046

Dixon, N., Spriggs, M. P., Smith, A., Meldrum, P., & Haslam, E. (2015). Quantification of reactivated landslide behaviour using acoustic emission monitoring. *Landslides*, *12*(3), 549–560. https://doi.org/10.1007/s10346-014-0491-z

Fredlund, D. G., & Rahardjo, H. (1993). *Soil Mechanics for Unsaturated Soils*. Wiley. https://doi.org/10.1002/9780470172759

Froude, M. J., & Petley, D. N. (2018). Global fatal landslide occurrence from 2004 to 2016. *Natural Hazards and Earth System Sciences*, *18*(8), 2161–2181. https://doi.org/10.5194/nhess-18-2161-2018

Gariano, S. L., & Guzzetti, F. (2016). Landslides in a changing climate. *Earth-Science Reviews*, *162*, 227–252. https://doi.org/10.1016/j.earscirev.2016.08.011

Guzzetti, F., Peruccacci, S., Rossi, M., & Stark, C. P. (2007). Rainfall thresholds for the initiation of landslides in central and southern Europe. *Meteorology and Atmospheric Physics*, *98*(3–4), 239–267. https://doi.org/10.1007/s00703-007-0262-7

Guzzetti, F., Peruccacci, S., Rossi, M., & Stark, C. P. (2008). The rainfall intensity–duration control of shallow landslides and debris flows: an update. *Landslides*, *5*(1), 3–17. https://doi.org/10.1007/s10346-007-0112-1

Hungr, O., Leroueil, S., & Picarelli, L. (2014). The Varnes classification of landslide types, an update. *Landslides*, *11*(2), 167–194. https://doi.org/10.1007/s10346-013-0436-y

India Meteorological Department. (2023). *Climatological tables of observatories in India. IMD, New Delhi*.

Intrieri, E., Gigli, G., Casagli, N., & Nadim, F. (2013). Brief communication "Landslide Early Warning System: toolbox and general concepts" *Natural Hazards and Earth System Sciences*, *13*(1), 85–90. https://doi.org/10.5194/nhess-13-85-2013

Iverson, R. M. (2000). Landslide triggering by rain infiltration. *Water Resources Research*, *36*(7), 1897–1910. https://doi.org/10.1029/2000WR900090

Koerner, R. M., McCabe, W. M., & Lord, A. E. (1978). Acoustic Emission Monitoring of Soil Stability. *Journal of the Geotechnical Engineering Division*, *104*(5), 571–582. https://doi.org/10.1061/AJGEB6.0000629

Kumar, D., Mahapatro, A. K., & Singh, S. K. (2024). Active waveguide deformation dynamics using acoustic emission technology for landslide early warning system. *Bulletin of Engineering Geology and the Environment*, *83*(2), 68. https://doi.org/10.1007/s10064-024-03548-6

Kumar, D., Mahapatro, A. K., & Singh, S. K. (2025). Assessing landslide velocity scales with acoustic emission active waveguides for early warning system. *Natural Hazards*. https://doi.org/10.1007/s11069-025-07316-x

Liu, Y., Cao, S., Du, S., Che, C., Wang, K., Zhao, C., Li, J., & Ma, R. (2025). Impact of water saturation on the deterioration of mechanical properties and damage mechanisms of sandstone composites. *Nondestructive Testing and Evaluation*, *40*(12), 5776–5803. https://doi.org/10.1080/10589759.2024.2449492

Lu, N., & Likos, W. J. (2006). Suction Stress Characteristic Curve for Unsaturated Soil. *Journal of Geotechnical and Geoenvironmental Engineering*, *132*(2), 131–142. https://doi.org/10.1061/(ASCE)1090-0241(2006)132:2(131)

Marin, R. J., & Velásquez, M. F. (2020). Influence of hydraulic properties on physically modelling slope stability and the definition of rainfall thresholds for shallow landslides. *Geomorphology*, *351*, 106976. https://doi.org/10.1016/j.geomorph.2019.106976

Michlmayr, G., Cohen, D., & Or, D. (2012). Sources and characteristics of acoustic emissions from mechanically stressed geologic granular media — A review. *Earth-Science Reviews*, *112*(3–4), 97–114. https://doi.org/10.1016/j.earscirev.2012.02.009

Petley, D. N., Mantovani, F., Bulmer, M. H., & Zannoni, A. (2005). The use of surface monitoring data for the interpretation of landslide movement patterns. *Geomorphology*, *66*(1–4), 133–147. https://doi.org/10.1016/j.geomorph.2004.09.011

Piciullo, L., Calvello, M., & Cepeda, J. M. (2018). Territorial early warning systems for rainfall-induced landslides. *Earth-Science Reviews*, *179*, 228–247. https://doi.org/10.1016/j.earscirev.2018.02.013

Segoni, S., Piciullo, L., & Gariano, S. L. (2018). A review of the recent literature on rainfall thresholds for landslide occurrence. *Landslides*, *15*(8), 1483–1501. https://doi.org/10.1007/s10346-018-0966-4

Smith, A., & Dixon, N. (2015). Quantification of landslide velocity from active waveguide–generated acoustic emission. *Canadian Geotechnical Journal*, *52*(4), 413–425. https://doi.org/10.1139/cgj-2014-0226

Smith, A., Dixon, N., & Fowmes, G. J. (2017). Early detection of first-time slope failures using acoustic emission measurements: large-scale physical modelling. *Géotechnique*, *67*(2), 138–152. https://doi.org/10.1680/jgeot.15.P.200

Smith, A., Dixon, N., Meldrum, P., Haslam, E., & Chambers, J. (2014). Acoustic emission monitoring of a soil slope: Comparisons with continuous deformation measurements. *Géotechnique Letters*, *4*(4), 255–261. https://doi.org/10.1680/geolett.14.00053

Stähli, M., Sättele, M., Huggel, C., McArdell, B. W., Lehmann, P., Van Herwijnen, A., Berne, A., Schleiss, M., Ferrari, A., Kos, A., Or, D., & Springman, S. M. (2015). Monitoring and prediction in early warning systems for rapid mass movements. *Natural Hazards and Earth System Sciences*, *15*(4), 905–917. https://doi.org/10.5194/nhess-15-905-2015

Terzaghi, K. (1943). *Theoretical Soil Mechanics*. Wiley. https://doi.org/10.1002/9780470172766

Vashista, S., Agrawal, A., Kaur, R., & Singh, S. K. (2025). Acoustic emission active channel intruder detection system based on machine learning. *Nondestructive Testing and Evaluation*, 1–24. https://doi.org/10.1080/10589759.2025.2560600

Vashista, S., Kumar, D., Kaur, R., Agrawal, A., & Kumar Singh, S. (2024). IoT-Based Landslide Detection System. In *Interdisciplinary Research in Technology and Management* (pp. 491–497). CRC Press. https://doi.org/10.1201/9781003430469-57

Wu, Q., Liu, Y., Tang, H., Kang, J., Wang, L., Li, C., Wang, D., & Liu, Z. (2023). Experimental study of the influence of wetting and drying cycles on the strength of intact rock samples from a red stratum in the Three Gorges Reservoir area. *Engineering Geology*, *314*, 107013. https://doi.org/10.1016/j.enggeo.2023.107013

Xu, R., Hu, Y., Yan, Z., Zhao, Y., & Li, Z. (2024). Experimental Investigation on the Effect of Water Saturation on the Failure Mechanism and Acoustic Emission Characteristics of Sandstone. *International Journal of Geomechanics*, *24*(6). https://doi.org/10.1061/IJGNAI.GMENG-8526